PUBLISHED VERSION:
De Taeye, L.L.; Vereecken, P.M. Chemo-mechanical effect of chlorine modified TiO2 coatings on LMO. J. Mater. Chem. A 2022, 10, 24398–24409 DOI: 10.1039/d2ta06009d

Chemo-Mechanical Effect of Chlorine Modified TiO_2 Coatings on LMO

Louis L. De Taeye*,† and Philippe M. Vereecken†,‡

†*Imec, Kapeldreef 75, 3001 Leuven, Belgium*

‡*KU Leuven, Department of Microbial and Molecular Systems, cMACs, 3000 Leuven, Belgium*

E-mail: Louis.DeTaeye@imec.be

Abstract

A thin-film model electrode was used to evaluate the performance of lowly and highly chlorine modified TiO_2 coatings. The coatings are applied using ALD on RF sputtered $LiMn_2O_4$ thin-films. Careful analysis of the ALD process indicates direct interaction between the precursor and the active material, leading to the formation of an interphase layer containing a high concentration of chlorine. Distinct differences in the performance of the two types of coatings arise dependent on the insertion potential (i.e. 3V or 4V insertion region) which was being evaluated. A link to the mechanical properties of the coating materials is hypothesized and evaluated using nanoindentation for mechanical assessment of TiO_2 and chlorine modified TiO_2.

Keywords

Li-ion rechargeable battery, TiO_2, thin-film, electrode coating, chlorine modification

1 Introduction

Spinel based cathode materials offer high rate performance thanks to the three dimensional Li-ion diffusion pathways, allowing easy movement of the ions inside the materials.[1] Furthermore, spinel cathodes allow all Li-ions to be extracted from the material without oxygen release or irreversible phase changes, as opposed to more commonly used layered electrodes, from which only a fraction of the total Li-ions can be extracted.[2] In this work, a commonly used spinel cathode, $LiMn_2O_4$, is studied. There are two distinct insertion potential regions in $Li_xMn_2O_4$. The first insertion potential region is situated around 4.1 V vs. Li^+/Li and corresponds to lithiation of γMn_2O_4 up to $LiMn_2O_4$. Further lithiation is observed around 2.9 V vs. Li^+/Li with lithiation up to $Li_2Mn_2O_4$.[3] The theoretical insertion capacities of both insertion regions are the same and correspond to 1Li-ion/2Mn atoms. Using both insertion regions extends the 630 mAh/cm^3 insertion capacity at 4.1V vs. Li^+/Li (labelled 4V region) with an additional 630 mAh/cm^3 at 2.9V vs. Li^+/Li (labelled 3V region).[3] Despite its potential as a high energy cathode, LMO continues to be troubled by both intrinsic lattice instability, manganese dissolution and electrolyte decomposition at potentials exceeding 4 V vs. Li^+/Li.

LMO is generally not discharged to $Li_2Mn_2O_4$, due to lattice instability. A cubic to tetragonal transition is observed in $Li_xMn_2O_4$ as $x>1$,[4] known as Jahn-Teller(JT) distortion. The lattice expands uniaxially by around 16% during JT distortion.[5] Repeated cycling in the 3 V insertion region leads to mechanical breakage, i.e. cracking of the active material, greatly reducing the cyclability.[3]

A second issue is transition metal dissolution. Mn^{+III} can dissolve from the electrode through a disproportionation reaction: $2\,Mn^{+III} \leftrightarrow Mn^{+II} + Mn^{+IV}$. Lithiation up to $x = 2$ shifts this reaction to the right, effectively increasing the rate of transition metal dissolution.[6]

A final critical barrier for successful commercialization of high energy cathodes is decomposition of the commonly used carbonate electrolytes at potentials exceeding 4V.[7] **The potential at which LMO is completely delithiated leads to electrolyte decompo-**

sition through oxidation of the solvent molecules,[8] both on the active material, the current collector, and any electronically conductive additives. Protons generated through electrolyte decomposition increase the rate of transition metal dissolution.[9] The rate of both transition metal dissolution and electrolyte decomposition scale with the surface area of the electrode/electrolyte interface.[10] Consequently, reducing the active material particle size in composite electrodes would aggravate the effect.

In this work the aforementioned issues in LMO will be tackled through surface engineering by application of a modified amorphous TiO_2 electrode coating. This strategy serves to shield the active material from the electrolyte solution, thereby mitigating electrolyte decomposition.[8]

A plurality of electrode materials have been coated with TiO_2 coatings in the past. Xiao et al. deposited 20 nm of TiO_2 on $0.5Li_2MnO_3$-$0.5LiNi_{0.5}Mn_{0.3}Co_{0.2}O_2$ by ultrasonification of TiO_2 nanocrystallites in alcohol, followed by annealing at 500°C for 6 hours.[11] This did not result in a conformal coating, but rather a porous structure of crystallites. Li et al. deposited TiO_2 on NMC111 through hydroxylation of $Ti(OBut)_4$, followed by annealing at 500°C for 5 hours. While minor improvements in the electrochemical performance of NMC were observed, the exact coating thickness and conformality were not assessed.[12] Zhao et al. coated NMC811 with anatase TiO_2. The crystallization required a high temperature step with the best performance observed after annealing at 550°C for 3 hours.[13] Substantial improvements of the cycle life, rate performance and high specific capacity were observed in Li-rich Li_2MnO_3 after the addition of an anatase TiO_2, which was claimed to suppress transition metal dissolution by mitigating the HF attack. The deposition of the coating required a thermal step of 450 °C.[14] The performance of the aforementioned coatings is dependent on the high temperature thermal treatment. While this methodology is feasible when the coating is applied directly on the active material, lower temperature processing is required to deposit coatings on top of complete composite electrodes (i.e. electrodes containing a conductive carbon additive and binder). Coating not only the active material, but

also the additives was shown to improve the overall performance these battery cells.[15] **A lower temperature process (130 °) was studied by Mattelaer et al.,[16] using an ALD process based on a tetrakis(dimethylamido)titanium (TDMAT) precursor and water as a reactant**. Herein, the performance of LMO was improved by reducing the amount of electrolyte decomposition and subsequent decomposition film formation at the electrode interface.

TiO_2 coatings were not only studied on cathode materials. Yang et al.[17] conducted a comparative study of crystalline and amorphous TiO_2 coatings on top of a Si anode. The amorphous TiO_2 coating exhibited a higher rate performance than the crystalline counterpart, due to the heightened Li^+-ion diffusivity.[18] In their work, the benefit of the amorphous material's elasticity was demonstrated, wherein it could accommodate a 77% expansion of the particle diameter. While the volume expansion in LMO is limited (16% uniaxial expansion) as compared to a Si anode (up to 400%), the coatings should still be able to withstand this expansion.

A variety of techniques are commonly used to deposit coatings on electrodes, such as chemical solution deposition, sol-gel, atomic layer deposition, co-precipitation, and solvo-thermal technique.[19] In this work, ALD will be used to deposit amorphous chlorine modified TiO_2 electrode coatings. While the use of ALD for electrode coatings is widespread,[20] some care needs to be taken with regards to direct reactions between the precursors and the active material. **Chen et al. conducted in-depth research of ALD deposition of Al_2O_3, based on a $Al(CH_3)_3$ precursor.** In their work they found that -OH groups are largely absent on the LMO surface. Consequently, the first cycles of ALD deposition react in a distinct manner, through decomposition of $-CH_3$, with corresponding formation of C_2H_6 and CH_4, during the first few cycles of ALD on LMO. The decomposition of CH_3 was in competition with the TMA/H_2O cycles. This process led to the partial reduction of Mn to +III at the surface, accompanied by Al doping.[21] A similar study has not yet been conducted using $TiCl_4$/H_2O cycles.

Battery electrodes are composite systems, containing binder, carbon black and infiltration of electrolyte in the electrode porosity.[22] This leads to an expansive parameter space which has to be optimized.[23] In this work, a thin-film electrode is used as a model system for a complete composite battery. This thin-film system has a well controlled thickness and morphology. As the thickness of the active materials is limited, no electronically conductive additive, nor porosity is required to establish good electronic and ionic contact, respectively. The controlled morphology simplifies conformal deposition of ALD and enables thin-film characterization techniques, such as Rutherford backscattered (RBS) and elastic recoil detection (ERD), to determine the material composition. Furthermore, LMO thin-films have been shown to exhibit outstanding rate performance.[24]

A comparative analysis will be made between lowly and highly chlorine modified TiO_2 coatings. In previous work, amorphous TiO_2 and chlorine modified TiO_2 were deposited by controlling the reactor temperature during ALD, using the $TiCl_4$ precursor and H_2O as a reactant. Chlorine modification was shown to be beneficial to TiO_2 as an anode material due to the enhanced Li-ion diffusion coefficient[25] and introduction of a conversion reaction at low potentials.[26] The addition of thicker coatings generally leads to increased Coulombic efficiencies, however severe loss of capacity is observed when the coatings become too thick.[16,27] Therefore coatings of different thickness will be assessed. A comparative study of the mechanical properties of both the highly chlorine modified and poorly chlorine modified TiO_2 films will be conducted.

2 Experimental Section

LMO was deposited using RF sputtering on a Kurt J. Lesker sputter tool, connected to a Ar filled glovebox, using a 3" LMO target (99.5% purity - Kurt J. Lesker). target Plasma ignition was achieved at a forward power of 40W, using an Ar flow at a pressure of 10 mTorr. After ignition the power was ramped up to the deposition power

of 55W at a rate of 0.033W/s. Deposition was done using Ar at a pressure of 3 mTorr. A 10 minute pre-sputtering was done before the shutter was opened and the sample substrate was exposed to the plasma. After deposition, the samples were stored in an argon filled glovebox. Annealing was done in a Thermo-Scientific F6000 Furnace in ambient. The heating rate was fixed at 5°C/min. An annealing temperature of 700°C was applied for 1 hour, followed by inactive cooling down to room temperature. After annealing the samples were brought back and stored in a Ar filled glovebox before electrochemical characterization or application of the coating.

The coatings were applied by ALD using a $TiCl_4$ (Pegasus Chemicals) **precursor and H_2O as a reactant in a Picosun ALD reactor at reactor temperatures of 50°C and 130°C.** A pulsing time of 0.2 seconds and 0.5 seconds is used for the $TiCl_4$ precursor and H_2O precursor, respectively, based on prior work.[25,26]

The spinel structure of the sputtered LMO films was determined by grazing-incident X-ray diffraction (GI-XRD) (X'Pert Panalytical) using a Cu Kα beam ($\lambda = 0.154$ nm). The observed peaks were associated with the corresponding materials using X-Pert Highscore. RBS was used to determine the absolute concentration of manganese, titanium and chlorine atoms in the deposited films. An incident 40 nA He^+ beam with a beam energy of 1.523 MeV was used. The analysis was performed using in-house developed software. The uncertainty in the RBS analysis is the sum of the counting statistical uncertainty and systematic errors. Systematic errors include uncertainties in the beam energy, detector energy calibration, measurement geometry, fitting algorithms, and uncertainties in the tabulated stopping powers.

ERD was used to determine the composition of the sputtered LMO films. ERD was conducted using a primary ion beam of $^{35}Cl^{4+}$ accelerated to 8 MeV by a 2 MV tandem accelerator. The forward recoiled and scattered ions were detected with a Time of flight – Energy (ToF-E) telescope. The telescope has a length of 845 mm, and was installed at a forward scattering angle of 38.5 °. The effect of elemental losses resulting from the interactions between the sample and the ion-beam was reduced by varying the target locations

on the sample (as opposed to focusing on one spot) during the measurement. A total of 10 different beam spot locations were measured on each sample. The lithium signal has been deduced from ^{7}Li and was corrected with its natural abundance.

XPS measurements were carried out in Angle Integrated mode using a QUANTES instrument from Physical Electronics. The measurements were performed using a monochromatized photon beam of 1486.6 eV on a 100 micron spot. The XPS spectra were charge corrected by setting the C 1s peak to a binding energy of 284.8 eV.

Nanoindentation was used to assess the difference in mechanical properties of TiO_2 and chlorine modified TiO_2. Nanoindentation was done on a Hysitron TI950 Triboindenter, using a pyramidal tip. 300 nm thick films were fabricated for nanoindentation, to minimize the substrate effect.

2.1 Electrochemical measurements

All electrochemical measurements were conducted using a custom built three-electrode Teflon cell. The Teflon cell consists of a vertical open-ended compartment and second semi-open-ended compartment. The two compartments are connected by a horizontal capillary to enable ion exchange. The thin-film working electrode is placed underneath the open-ended compartment. A DuPont Kalrez O-ring was used to prevent electrolyte leakage from the Teflon cell over the working electrode. The nominal value of the O-ring diameter is 8.9 mm (0.68 cm^2), however, the diameter of the exposed area was measured to be 10 mm (0.78 cm^2). Lithium ribbons are placed into the open ends of both vertical compartments and serve as counter and reference electrode.

A 0.94M $LiClO_4$ solution was made by adding propylene carbonate (PC) (anhydrous, Sigma-Aldrich) to 10 g of $LiClO_4$ (battery grade, dry, 99.99%, Sigma Aldrich) to make the final 100 ml electrolyte solution. The electrolyte was prepared and stored in an argon filled glovebox to prevent contamination by moisture or air.

The electrochemical measurements were conducted using a Metrohm M101 potentiostat, which was operated using the Metrohm Nova software package. All measurements were conducted inside an Ar filled MBraun glovebox (O_2 and H_2O content <0.1 ppm).

3 Results and Discussion

3.1 Thin-film Deposition and Characterization

ERD measurements were done to determine the stoichiometry of the annealed LMO film. A Li to Mn ratio of 0.481 ± 0.048 and an O to Mn ratio of 1.955 ± 0.152, corresponding well with the targets of 0.5 and 2 for $LiMn_2O_4$, were measured. Only trace amount of H and C were observed at the LMO surface, with atomic fractions around 1% for both elements. The spinel phase of LMO was observed using XRD.

An areal Mn density of $251.6 \pm 5.7 \times 10^{15}$ at/cm^2 was measured using RBS. This manganese content corresponds to an equivalent thickness of 88 nm, calculated using the mass density of 4.01 g/cm^3 and molecular mass of 180.8 g/mol. The current applied during galvanostatic charge-discharge was normalized to the absolute Mn content. This is achieved by dividing the total charge required to reduce/oxidize the total Mn content by the charging time. The volumetric capacity is calculated based on the equivalent electrode thickness (i.e. 88 nm).

Thin-films of TiO_2 were deposited using an ALD process, based on $TiCl_4$ as a precursor and H_2O as the reactant. Under equilibrium conditions, this deposition process is described as:[25]

$$n(M-OH) + TiCl_4 \leftrightarrow (M-O-)TiCl_{4-n} + nHCl \tag{1}$$

An OH terminated surface reacts with the $TiCl_4$ precursor, forming both HCl and a chlorine terminated surface layer in the process. The H_2O exposure interacts with the chlorine

terminated surface as:

$$(M-O-)TiCl_{4-n} + (4-n)H_2O \leftrightarrow (M-O-)Ti(OH)_{4-n}) + (4-n)HCl \qquad (2)$$

Complete removal of chlorine in eq. (2) is ensured if the system is given enough time to equilibrate. Lowering the reactor temperature causes divergence from ideal conditions, leading to incomplete Cl removal.[26] Furthermore, as noted by,[21] LMO is not completely -OH terminated, which means the first steps fundamentally differ from this ideal situation.

RBS was used to determine the extent of the chlorine incorporation at different temperatures in previous work.[26] In this work two types of chlorine modified TiO_2 will be assessed as an electrode coating: $TiO_2Cl_{0.04}$, deposited at 130 °C and $TiO_{1.9}Cl_{0.19}$, deposited at 50 °C. **The choice of these conditions is based on former work[25,26] where a correlation between the chlorine content, the diffusion coefficient of Li-ions through the material, and insertion capacity of the material was described. The two temperatures were chosen as they lead to a significant difference in chlorine content in the film.** These types will be labelled TiO_2 - reflecting the relatively low chlorine modification -, and TiO_2Cl, respectively.

3.2 Characterization of the LMO/TiO_2 interface

As the H concentration at the surface of LMO is negligible, the first steps in the ALD process may fundamentally differ from the ideal conditions as described in eq. (1). Therefore, the thickness and composition of the coating needs to be re-evaluated when deposited on LMO.

RBS was used to calculate the coating thickness from the areal atomic concentration of Ti. This methodology was used both on 3 nm and 5 nm coatings, as thinner coating are outside the limit of detection of RBS. The thickness was based on an atomic concentration of 2.65 $\times$ 10^{15} Ti atoms/cm$^2 \cdot$ nm, which was calculated in previous work[26] for TiO_2. TiO_2 coating thicknesses of 4.83 nm (target 5 nm) and 2.53 nm (target 3 nm) were obtained. The thickness

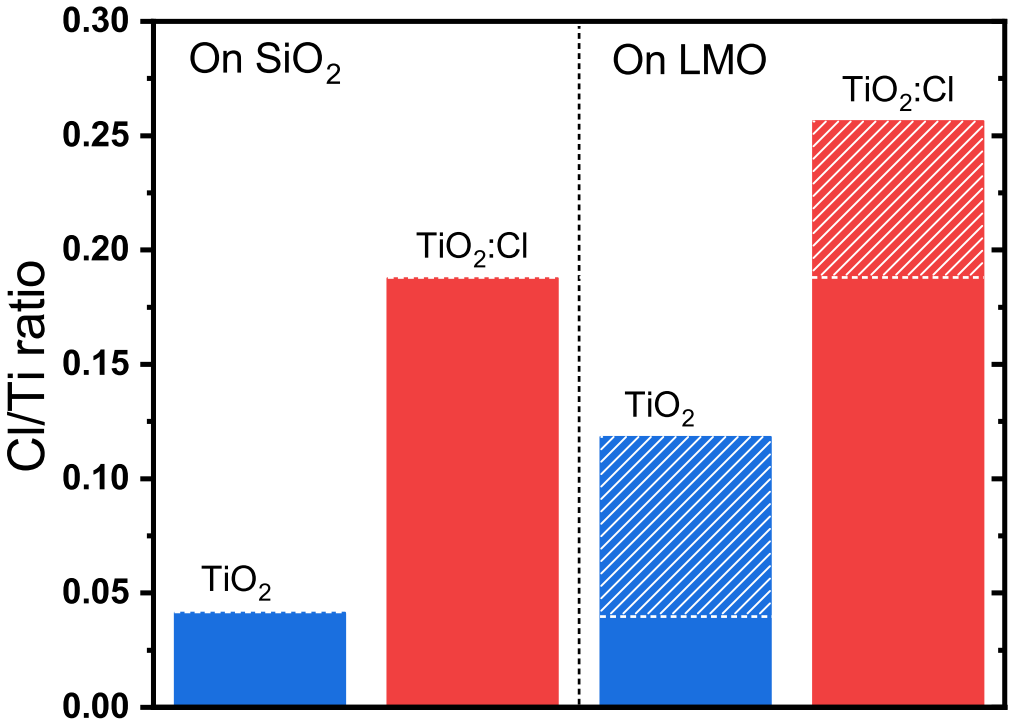

Figure 1: Comparison of the chlorine to titanium ratio of TiO_2 deposited at 130°C (blue) and 50°C (red) on SiO_2 (as measured in previous work[26]) and when the material is deposited as an electrode coating on LMO.

of TiO_2Cl coatings were calculated in the same way, where thicknesses of 5.69 nm (target 5 nm) and 2.78 nm (target 3 nm), were obtained. The RBS measurement shows a large discrepancy between the actual and expected chlorine content. The resulting ratio is plotted in figure 1, alongside the ratio determined in previous work. Strikingly, the Cl/Ti ratio in 5 nm TiO_2 and TiO_2Cl deposited on LMO is significantly higher than the ratio measured when the coating was deposited on SiO_2. The areal concentration of the excess chlorine corresponds to 98×10^{13}at/cm^2 and 99×10^{13}at/cm^2 for TiO_2 and TiO_2Cl, respectively. As discussed in the previous section, the absence of -OH groups may affect the first cycles of the ALD process. This will affect both the growth rate and the film composition. The RBS data suggests the presence of a chlorine rich layer, which will likely be found at the LMO/TiO_2(Cl) interface.

Two additional experiments were executed to assess whether this layer does indeed form at the LMO interface. In the first experiment, the electrode coatings was scaled down to 1 nm, below the detection limit of RBS. XPS was used to verify the presence of a chlorine rich layer at the LMO/TiO_2 interface, the effect of which will be more pronounced in thinner films. Table 1 (top) shows the surface composition calculated from the XPS spectra. The layers deposited at 50°C and 130°C have almost exactly the same stoichiometry. This is likely caused by the chlorine rich layer at the LMO/TiO_2(Cl) interface. Furthermore, the fraction of Ti in the measured signal is similar, suggesting the same film thickness was obtained, i.e. the temperature did not have a major impact on the composition and mechanism of the first ALD cycles.

Spectra of the different elements are shown in figure 2. Both the Mn 3s and Mn 2p spectra were recorded to determine the oxidation state of Mn. The magnitude of the energy splitting in the former is a diagnostic of the oxidation state. A splitting of 5.02 eV is recorded, corresponding most closely to Mn^{+IV} ($\sim$ 4.8 eV). The peak shape of the recorded Mn 2p resembles the peak shape of Mn^{+II}. Mn^{+II} generally shows a satellite peak around 647 eV, which could not be identified in this spectrum. A mixture of Mn^{+II} and Mn^{+IV} is likely

Table 1: **Table showing the atomic ratios (%) of all elements in 1 nm TiO_2 and TiO_2Cl films (top) and elemental ratios after prolonged $TiCl_4$ exposure (bottom) demonstrating the CVD like reaction between $TiCl_4$ and LMO.**

ALD cycling

Sample	Li 1s	C 1s	O 1s	Cl 2p	Ti 2p	Mn 2p
TiO_2Cl - 10 cycles	3.62	29.09	47.38	2.03	7.02	10.88
TiO_2 - 17 cycles	3.10	27.82	47.85	2.06	7.11	12.06

Precursor exposure (130°C)

Time (s)	Li 1s	C 1s	O 1s	Cl 2p	Ti 2p	Mn 2p
6	5.37	21.01	51.09	1.02	0.99	20.33
60	5.10	21.94	49.87	1.36	1.37	20.14
600	4.87	24.35	47.43	2.21	2.13	18.23

present at the surface.

The Ti 2p spectrum shows two peaks, corresponding to Ti $2\,p_{1/2}$ at 464.4 eV and Ti $2\,p_{3/2}$ at 458.7 eV binding energy, respectively. Peak splitting of 5.750 eV is measured, corresponding to the chemical state of TiO_2. Finally the Li spectrum is shown, where a small peak was observed, which likely corresponds to Li-ions in LMO at 53.9 eV. The peak at 62.8 eV in this same spectrum corresponds to Ti 3p.

Both the XPS and RBS signal measured on the coated LMO films suggest non-ideal behaviour during the first cycles of the ALD process. The high chlorine layer suggests the formation of a Cl rich film on top of LMO, after which the regular cycling, as described in eq. (1) and (2) is established. Here we propose the following mechanism:

$$TiCl_4 + 2LiMn_2O_4 \leftrightarrow TiO_2 + 3MnO_2 + 2LiCl + MnCl_2 \tag{3}$$

Wherein the $TiCl_4$ reacts with the active material forming LiCl and $MnCl_2$. This involves the reduction of 1 Mn atom from +III down to +II and oxidation of Mn from +III to +IV with the formation of MnO_2. The XPS spectra of Mn indicate the presence of Mn^{+II} after $TiCl_4$ exposure. In the initial state -

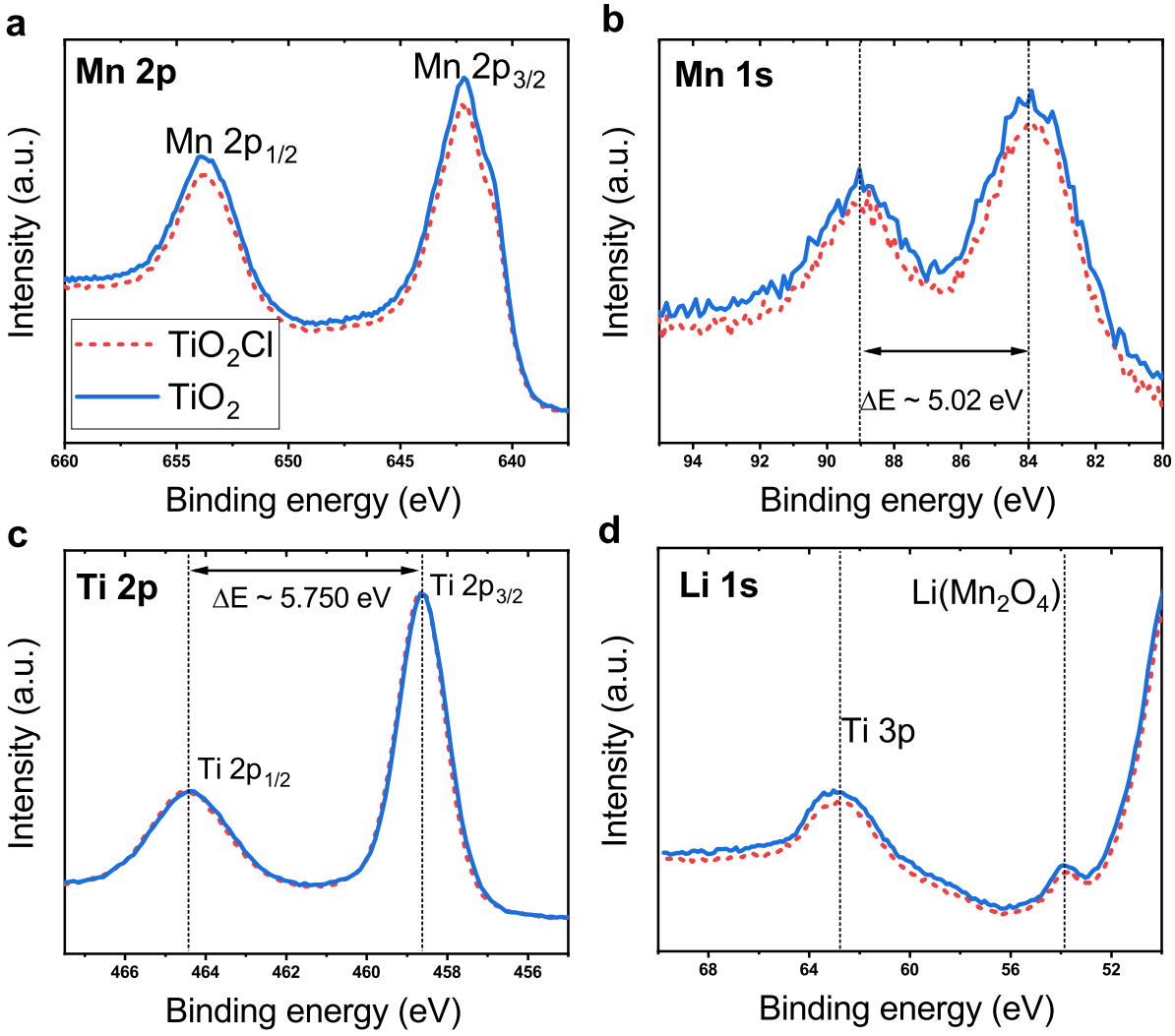

Figure 2: XPS measurement conducted on 1 nm coatings deposited at 50°C (TiO_2Cl) and 130°C (TiO_2).

prior to $TiCl_4$ exposure -, half the Mn atoms in the LMO film are in the +III state and half in the +IV (also confirmed by the composition measured by ERD: $Li^{+}Mn^{+III}Mn^{+IV}O_4^{-2}$). As such the Mn^{+II} forms during the interaction with the precursor and is likely linked to $MnCl_2$ formation. The LiCl signal was absent in the XPS spectrum, which may be caused by oxidation or hydrolysis of LiCl to LiOH or Li_2O during the H_2O exposure or after exposure to air.

To further assess whether direct interaction between the precursor and active material persists, the LMO electrode was exposed to a single exposure of $TiCl_4$ for a prolonged period of time, to asses whether a layer still forms. The exposure time was increased to 6 s, 60 s, and 600 s. The resulting elemental ratios are shown in table 1. Continuous growth of the surface layer was observed, as the measured Ti/Mn ratio increases with prolonged exposure times, which bolsters the hypothesis of a direct interaction between $TiOCl_4$ and $LiMn_2O_4$. **Furthermore, the continuous increase in the Ti content over the prolonged periods of time not only indicates a reaction takes place, but also that the reaction is not surface limited, but rather continues to interact with the LMO. As such, during the initial cycles we are not looking at ALD, but rather CVD-type behaviour. Naturally, this initial interaction will affect the conformality of the deposition and will influence the growth rate of the deposited films.**

3.3 Electrochemical performance of chlorine modified TiO_2-Coated LMO

As there are only minor compositional differences in 1 nm TiO_2 and 1 nm TiO_2Cl coatings, these two will not be assessed independently. The samples which were measured are a LMO reference, 1 nm, 3 nm, and 5 nm TiO_2Cl, and 3 nm and 5 nm TiO_2. A cyclic voltammogram (CV) was measured on each of these coated electrodes. The CV started from OCP followed by increasing the potential to the upper vertex potential of 4.35 V vs. Li^{+}/Li, after which the material was cycled 3 times between 2.4 V and 4.35 V at a scan rate of 10 mV/s. The

measurement was stopped at a potential of 4.25 V vs. Li^+/Li. The resulting current profile of the reference measurement and TiO_2 or TiO_2Cl coated samples are shown in figure 3. Three insertion processes can be distinguished in the LMO reference (black line). The insertion process in LMO is described as:

$$\delta x Li^+ + \delta x e^- + Li_x Mn_2 O_4 \leftrightarrow Li_{x+\delta x} Mn_2 O_4 \tag{4}$$

During the first cycle, the current profile on the anodic side in the 4 V region differs from the subsequent samples. Current peaks at 4.12 V and 4.25 V were observed in the first cycle, which shift down to 4.08 V and 4.21 V, respectively during subsequent cycles. The corresponding cathodic current peaks are observed at 3.89 V and 4.03 V, and were stable from this first cycle onward. The current peaks at the highest potential correspond to a stoïchiometry of $0 \leq x \leq 0.5$, the slightly lower insertion peak in the 4 V region corresponds to a stoïchiometry of $0.5 \leq x \leq 1$. The splitting of these two peaks is related to charge ordering in LMO at a composition with $x = 0.5$, beyond which the Li-ions segregate into tetragonal crystal sites.[28] The dissimilarity during the first cycle in the 4 V region and subsequent cycles was ascribed to irreversible changes in the bulk and surface of the active material.[29] The cathodic and anodic peaks at 2.67 V and 3.12 V, respectively, correspond with the insertion process between $1 \leq x \leq 2$.

The addition of a 3 nm or 5 nm TiO_2 coating drastically changes the current profile. The former only shows a small anodic peak at 3.42 V vs. Li^+/Li with a corresponding peak current of 32 $\mu A/cm^2$, significantly smaller than the peak current of 455 $\mu A/cm^2$ observed in the uncoated counterpart. No peaks were observed in the 4 V region. The addition of a 5 nm TiO_2 coating completely blocks the current flow.

The 1 nm TiO_2Cl coated film is shown in figure 3b. No anodic peak is observed during the first cycle, however, peaks attributed to Li^+ insertion are observed on the cathodic side during the reverse sweep. The current profile remains constant during consecutive cycles,

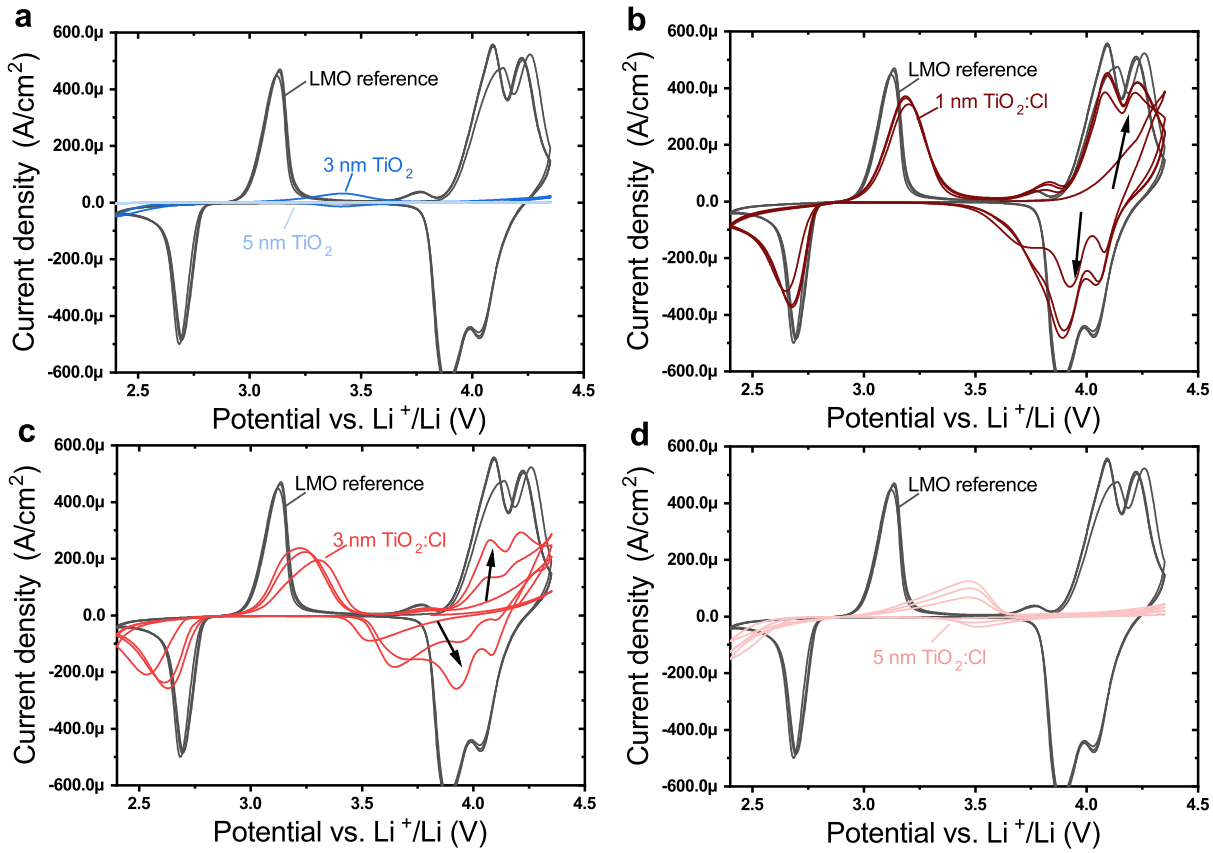

Figure 3: Cyclic measured on LMO coated with 3 nm and 5 nm TiO_2 (a), 1 nm TiO_2Cl (b), 3 nm TiO_2Cl (c), and 5 nm TiO_2Cl (d). The CV is measured between 2.4 V and 4.35 V vs. Li^+/Li at 10 mV/s.

after this initial cycle. The peak current and position differs from the uncoated counterpart, wherein each anodic peak shifted to the right and each cathodic peak to the left, indicative of increased internal resistance. The 3 nm TiO_2Cl coating took longer to activate than the 1 nm coated samples. Consecutive increases in the current density were observed with each cycle. During the first two cycles no anodic peaks were observed in the 4 V region. The Li-ion insertion peaks in the 4 V region shifted down to 3.52 V vs. Li/Li during the first cycle, and became indistinguishable. In the second cycle three peaks are observed at 3.65 V, 3.96 V, 4.06 V, respectively. The current peak at 3.65 V diminished in the third cycle, as the current peaks at 3.96 V and 4.06 V increase. In the 3 V region the current profile was stable after the first cycle, however, the current peak is substantially lower than the reference ($i_{a,peak}$ = 236 µA/cm^2 / $i_{c,peak}$ = -234 µA/cm^2 in the 3 nm coated sample versus $i_{a,peak}$ = 455 µA/cm^2 / $i_{c,peak}$ 478 µA/cm^2). The 5 nm TiO_2Cl coating blocks the current further, as no current peaks were observed in the 4 V region, the anodic current peaks in the 3 V region diminished further to 97 µA/cm^2, and no cathodic peak was observed.

The rate performance of each of the samples was measured using galvanostatic charge-discharge, immediately following CV. Currents are calculated based on the areal density of Mn, measured by RBS ($c_{Mn} = 251.6 \pm 5.7 \times 10^{15}$ at/cm^2). The total charge associated with a full charge/discharge step equals e × c_{Mn}. This corresponds to a current of 11.3 µA/cm^2 at 1C. The rate performance was measured using galvanostatic charge-discharge with potential cut-offs at 4.25 V and 2.4 V for the charge and discharge step, respectively. 4 cycles were measured at 1C, 0.5C, 2C, 5C, 10C, 20C, 50C, 100C, and 1C. The discharge steps are shown in figures 4a-b.

A low capacity was measured in the first discharge cycle, as this follows immediately after the cyclic voltammetry. During the first 8 cycles a slight increase in the capacity was observed in the reference sample. This is mainly attributed to the 3 V region, wherein the capacity increases slightly due to repeated straining.[30] After two cycles, the 3 nm TiO_2 coated LMO electrode obtains a capacity similar to that of the uncoated reference. This seems to suggest

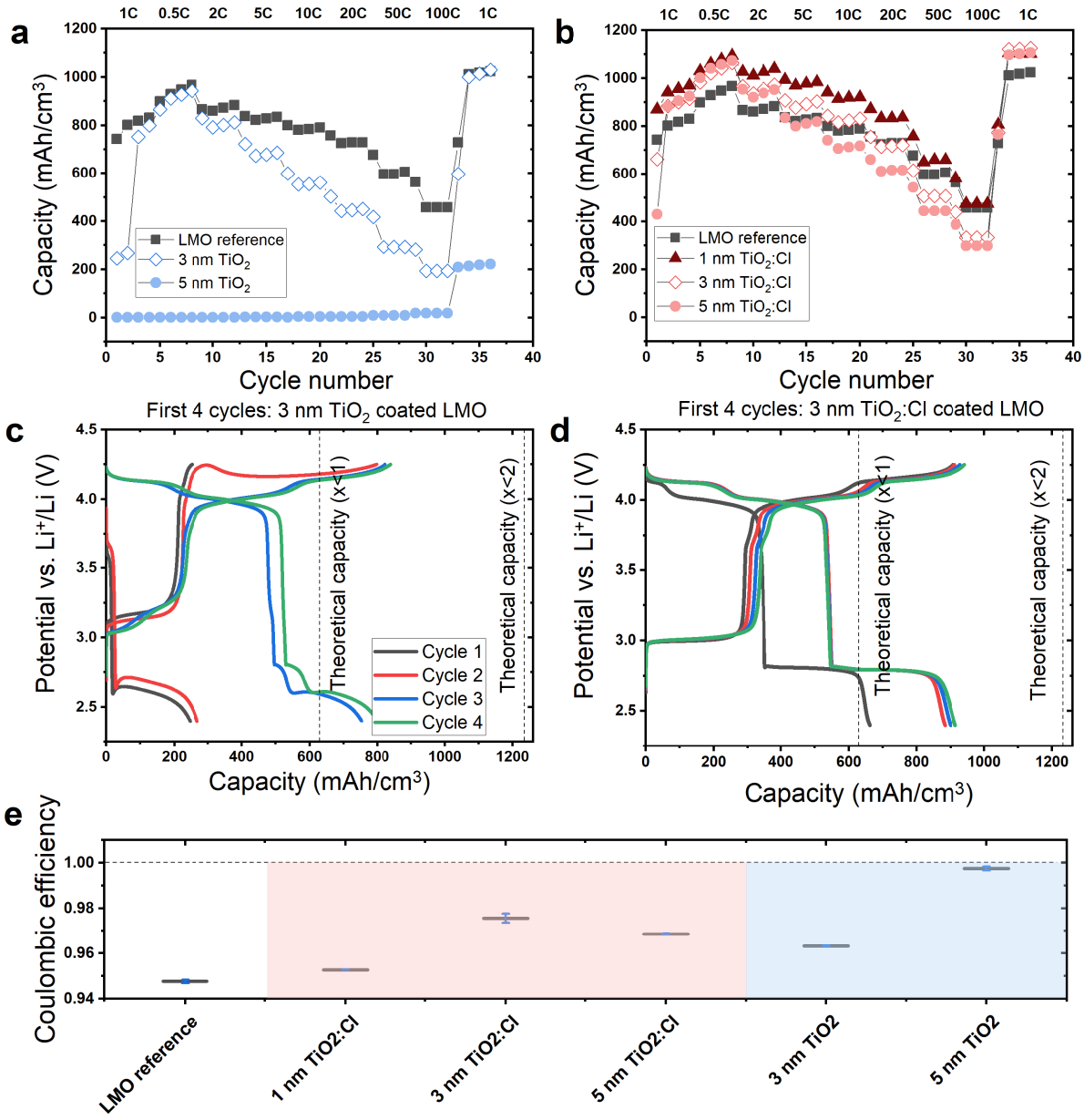

Figure 4: Galvanostatic charge-discharge measurements conducted on TiO_2(a) and TiO_2Cl(b) coated LMO. Charing rates ranging from 0.5C up to 100C were applied, where 1C = 11.3 µA/cm^2. The first cycles are shown for 3 nm TiO_2(c) and TiO_2Cl(d). The Coulombic efficiency in the final 4 cycles measured on each different sample is shown in (e).

a further decrease of the internal resistance of the cell during galvanostatic cycling. The first 4 cycles, measured at 1C, are shown in figure 4c. A small capacity is obtained for both the charging and discharging step in the first cycle, wherein no capacity is measured in the 4 V region. During the second charging step the potential is observed to peak and decrease around 300 mAh/cm^3. In subsequent cycles this behaviour is no longer observed. In the 3 V region, a small capacity ($\pm$ 50 mAh/cm^3) is observed at 2.8 V vs. Li$^+$/Li, followed by additional intercalation at 2.6 V vs. Li$^+$/Li. At higher C-rates, the capacity drops faster for the coated sample than for the uncoated reference, signifying a heightened internal resistance. The 5 nm coated electrode shows no capacity during the first 32 cycles, after which a small capacity of 200 mAh/cm^3 is observed in the 3 V region, hence the coating remains blocking to the ion flow.

The rate performance of the TiO_2Cl coated electrodes is substantially better than that of the TiO_2 coated electrodes. The addition of a TiO_2Cl coating increases the measured capacity by around 12% at 1C during the first cycles, independent of the coating thickness. As thicker coatings were deposited, the rate performance becomes progressively worse, with a reduction in the capacity of 53%, 56%, 69%, and 73%, as the rate is increased from 1C to 100C, for the reference sample, 1 nm, 3 nm, and 5 nm TiO_2Cl coated samples, respectively. Analysis of the first 4 cycles of the 3 nm TiO_2Cl coated electrode shows a flat plateau in the 3 V region and the two plateaus in the 4 V region from the first cycle onward, contrary to the profile observed in 3 nm TiO_2 electrode, where a second plateau became apparent in the 3 V region. Herein the initial lithiation occurred at the expected potential of 2.8 V, but further lithiation required a higher overpotential, down to around 2.5 V.

The Coulombic efficiency of (un)coated LMO is determined in the last 4 cycles of the galvanostatic charge-discharge experiments (as shown in figure 4(e)). The uncoated sample has a charging efficiency of 94.8%. This only increases to 95.3% after the application of a 1 nm TiO_2Cl coating. As the coating thickness is increased up to 3 nm and beyond a larger benefit in terms of Coulombic efficiency is observed, with values of 97.5% and 96.8% for 3 nm and

5 nm TiO_2Cl, respectively. An increase up to 96.3% is observed in the 3 nm TiO_2 coated electrode and the charging efficiency of 99.7% measured in the 5 nm TiO_2 sample is by far the highest, however, it should be noted that the capacity measured in these films is very small, consequently is not useful as an electrode coating.

The cyclic voltammograms after the charge-discharge measurements show large current peaks, where in the first CV (i.e. before galvanostatic charge-discharge) these current peaks were small or completely absent. The 3 nm TiO_2 coated LMO electrodes shows an electrochemical response to the changing applied potential, whereas only negligible currents are observed in the 5 nm TiO_2 coated LMO. For TiO_2Cl coatings the current profile almost exactly matches the uncoated reference, aside from the small difference in the anodic current flow around 3.9 V vs. Li^+/Li and a corresponding difference on the cathodic side at 3.6 V vs. Li^+/Li.

The size of the current peaks and peak potentials corresponding to each of the insertion ranges and with the addition of all different coatings are shown in Figure 5c-f. As the 5 nm TiO_2 coating blocks the insertion reaction, it is omitted from further analysis.

The peak potential is independent of the choice of coating, i.e. both the TiO_2 and TiO_2Cl coatings show constant peak potentials for each redox reaction, independent of the thickness of the coating. Interestingly, the magnitude of the current peaks scales inversely with the coating thickness. Figure 5e show the peak current density of TiO_2 coated LMO. A downwards trend is observed for each of the insertion processes. The 3 V insertion reaction is affected more drastically than the 4 V region reactions, as indicated by the steep decrease in the red curve from 505 $\mu A/cm^2$ for the LMO reference, down to 247 $\mu A/cm^2$ for LMO with a 3 nm TiO_2 coating. The current inhibition caused by a TiO_2Cl coating is less pronounced, wherein a decrease from 505 $\mu A/cm^2$ down to 399 $\mu A/cm^2$ was observed in the 3 V region and a decrease from 388 $\mu A/cm^2$ down to 339 $\mu A/cm^2$ in the 4 V region (these values correspond to the anodic peak current of each process). Despite the lower inhibition, the 3 V region was affected more by the addition of the coating than the 4 V region.

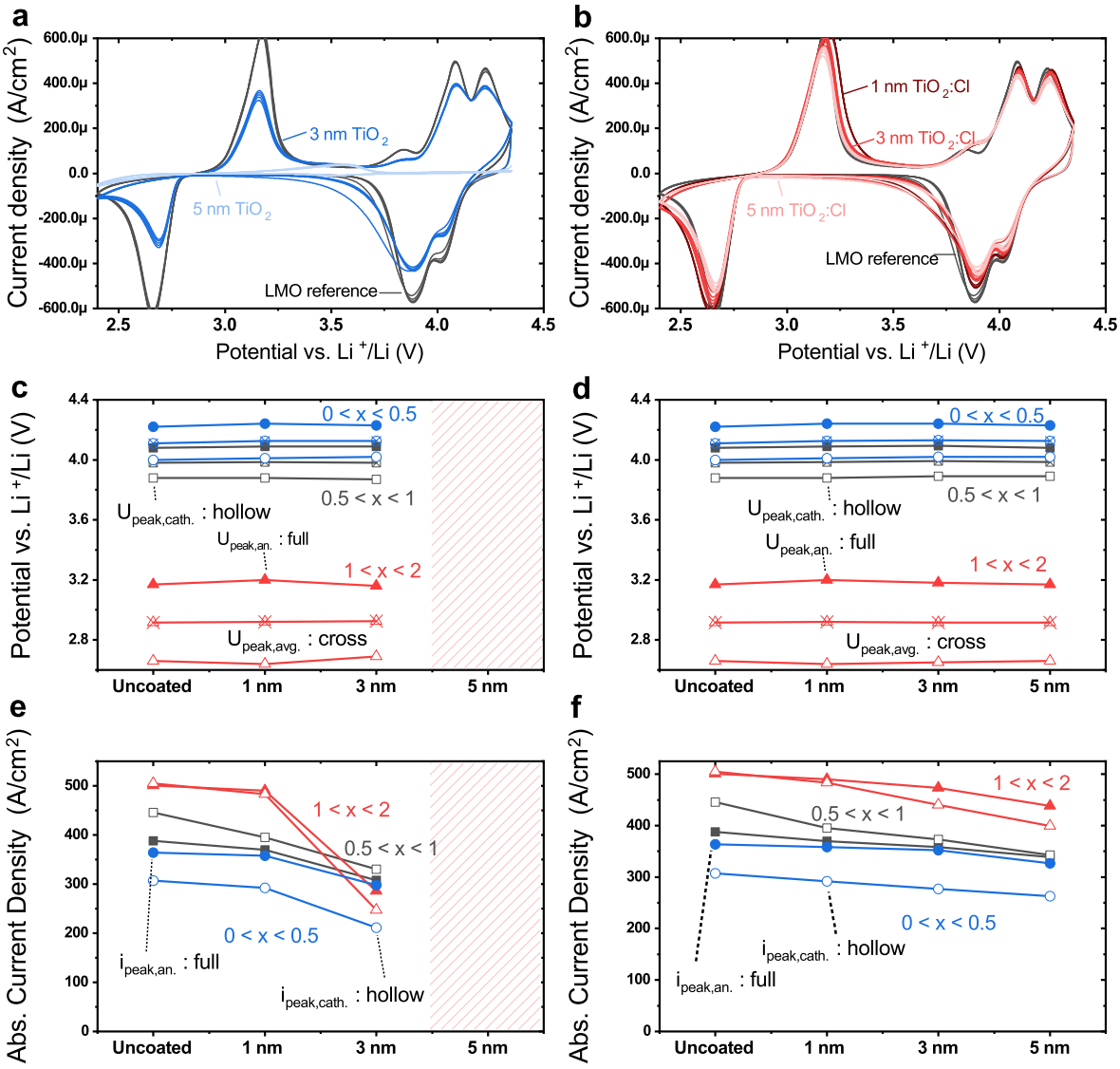

Figure 5: Cyclic measured between 2.4 V and 4.35 V vs. Li^+/Li at 10 mV/s on LMO coated with 3 nm and 5 nm TiO_2 (a), 1 nm TiO_2Cl, 3 nm TiO_2Cl (c), and 5 nm TiO_2Cl after galvanostatic charge-discharge (b). Peak potential corresponding to the current peaks, wherein the x value corresponds to the lithiation state of $Li_xMn_2O_4$ of TiO_2 (c) and TiO_2Cl (d) coated LMO. Peak current density of TiO_2 (e) and TiO_2Cl (f) coated LMO.

TEM images of the 5 nm TiO_2Cl sample were taken before and after the electrochemical measurements to determine whether changes have occurred in the electrode morphology, as shown in Figure 6. The measured thickness matches closely with the target thickness of 5 nm. Despite the significant change in the CV after the galvanostatic charge-discharge measurements, no clear change was observed in the electrode itself, nor in the electrode coating. EDS measurements verify the continued presence of the TiO_2Cl coating, which follows the LMO morphology. Both Ti and Cl are confined to the top of LMO.

The uniaxial lattice expansion of LMO, consequence of Jahn-Teller distortion, is associated

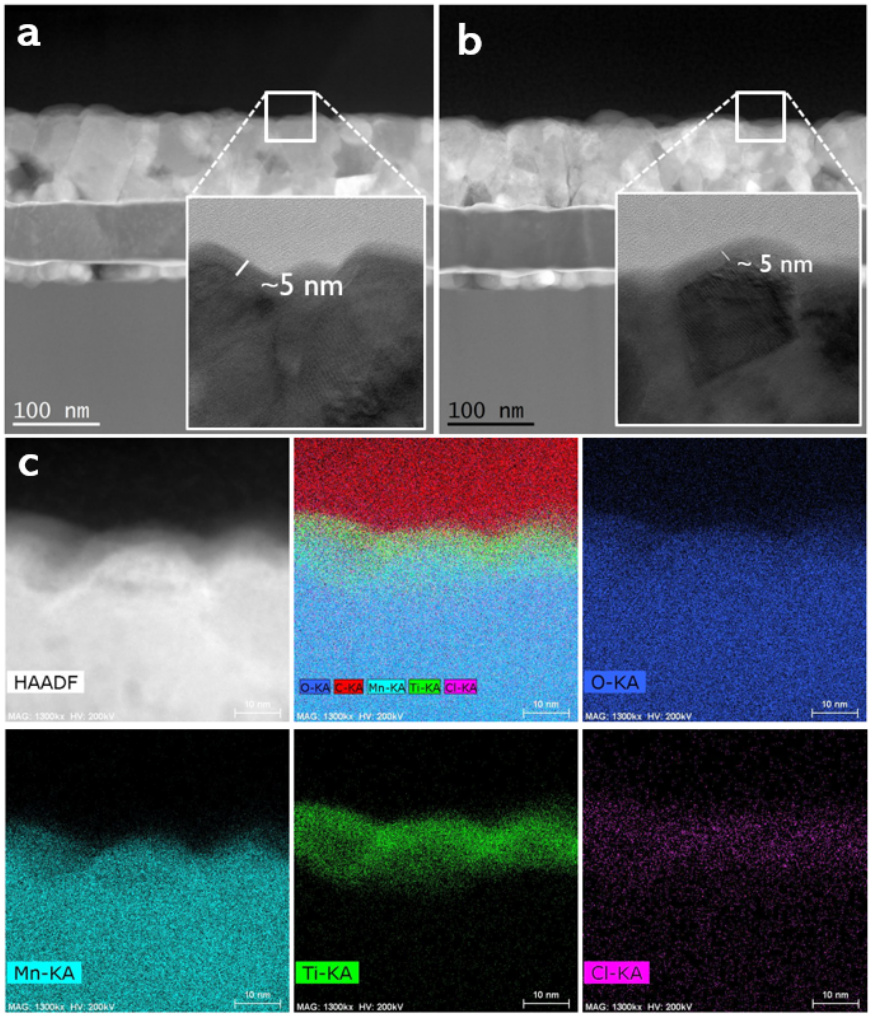

Figure 6: TEM images of 5 nm TiO_2Cl coated LMO before (a) and after (b) electrochemical measurements. (c) HAADF and EDS measurements of 5 nm TiO_2Cl coated LMO after electrochemical measurements.

with Li-ion insertion in the 3 V potential region. Electro-chemo-mechanical coupling caused by the coating could cause the observed behaviour, hence the mechanical properties of both types of coatings will be assessed using nanoindentation.

3.4 Comparative Study of Mechanical Properties of Chlorine Modified and Unmodified TiO_2

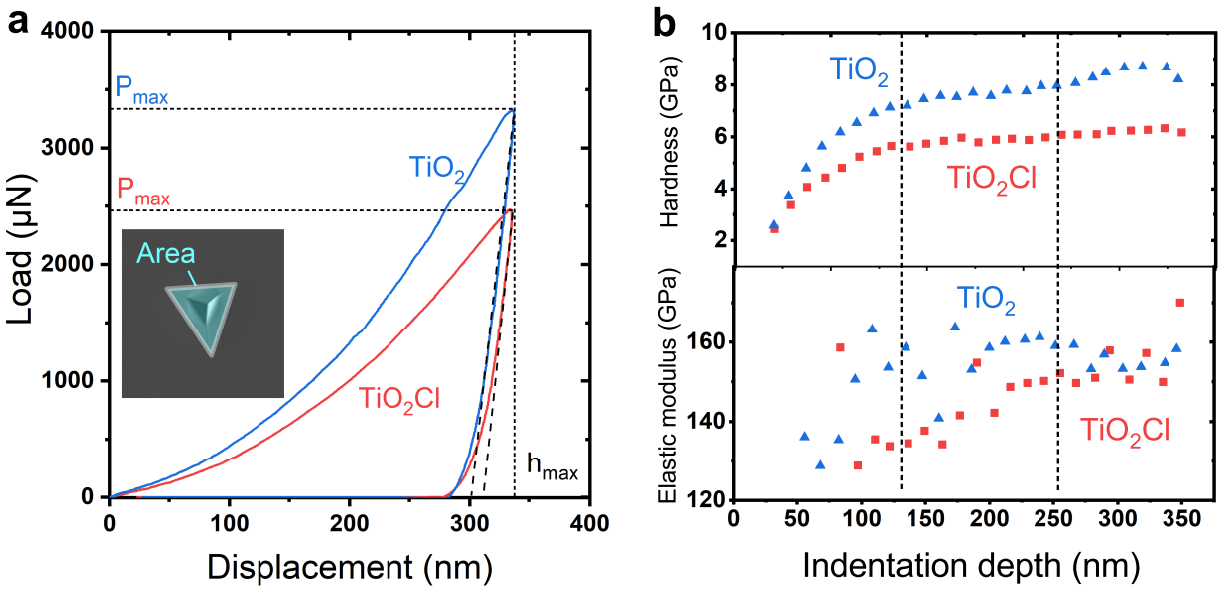

Figure 7: Results of nanoindentation, measured on 300 nm films: (a) Loading curves measured on TiO_2 and TiO_2Cl. (b) Hardness and elastic modulus measured on the same materials.

The hardness and elastic modulus of the two coating materials were determined using nanoindentation. Loading curves were measured containing the elasto-plastic behaviour of the material at different indentation depths. After each (un)loading curve was obtained, the crack length formed in the film is measured. The hardness was calculated as $H=P_{max}/A$ with P_{max} the pressure measured at the highest indentation depth and A the projected area of the imprint, as shown in Figure 7(a). The elastic modulus is determined from the slope

of the unloading profile at P_{max} as:

$$E = \frac{\sqrt{\pi}}{2}\frac{S}{\sqrt{A}} \tag{5}$$

with

$$S = \frac{dP}{dh}|_{P_{max}} \tag{6}$$

as described by Oliver and Pharr.[31] It should be noted that exact quantification of the elastic properties of amorphous materials using nanoindentation is difficult, due to the uncertainty in how layer accommodates the volume of material displaced by the indenter.[32] While more exact quantification is possible by including finite element modelling,[33] only the qualitative assessment is employed here.

The hardness, a measure of the materials resistance to plastic deformation is around 20% lower in highly chlorine modified TiO_2 than in the lower modified variant. Similarly, the elastic modulus is around 20 GPa lower in TiO_2Cl.

The difference in the properties of these two materials indicates that TiO_2Cl more easily deforms both plastically and elastically. This may be the root cause of the faster activation behaviour observed electrochemically, i.e. the film more easily deforms and contact stress is more easily released in the TiO_2Cl coated films, effectively enabling (de)lithiation. Thorough chemo-mechanical coupling can explain the disparity between the performance of the two coatings, as chemical expansion is an important parameter relating to material functionality.[34] The high hardness and elastic modulus could explain why the TiO_2 coating, which is more resilient to deformation, prevents effective lithiation in the 3 V region of LMO, by blocking the cubic to tetragonal transition. Increased stress on an electrode material was formerly shown to decrease the material's ability to strain as the composition changes, which in turn leads to decreased capacity.[35] This would explain the substantially higher internal resistance and lower capacity in the 3 V region than in the 4 V region. Naturally, the application of a conformal surface coating would aggravate the effect, as the addition of crystallites

as a coating would not increase the contact stress generation.

4 Conclusions

A comparative study of amorphous TiO_2 and TiO_2Cl coated LMO, operated in both the 3V and 4V region, was conducted in this work. The lowly and highly chlorine modified coatings were deposited using ALD on top of RF sputtered LMO thin-film electrodes. The chlorine modification was controlled by changing the reactor temperature during the ALD process. Prior to studying differences in electrochemical behaviour of samples coated with the two types of amorphous TiO_2, and with different coating thicknesses, the ALD process on LMO was evaluated. RBS measurements showed direct interaction between the LMO substrate and the $TiCl_4$ precursor, used during the ALD deposition, which leads to the formation of $MnCl_2$, LiCl, MnO_2 and TiO_2. Once a complete layer of TiO_2 is formed, the process can continue as described in equations (1) and (2). This interaction, and consequently the interlayer formation is independent of the reactor temperature, as no change in the material composition was observed between 1 nm thick coatings deposited at 50°C and 130°C. This shows the importance of evaluating any ALD process on the active material, rather than on 'well behaving' substrates, such as e.g. SiO_2, as the initial cycles might differ significantly. Chlorine modification of the coating substantially improves the electrochemical properties over those of the non-modified coated samples. The specific capacity in TiO_2Cl coated electrodes was higher than the uncoated counterpart at low C-rate (up to 2C), beyond which the rate performance of the uncoated film was better than the coated counterpart. 1 nm TiO_2Cl demonstrated the highest capacity. In terms of stabilization w.r.t. electrolyte decomposition, films exceeding 1 nm were required, as a coating with a thickness exceeding 3 nm increased the efficiency by $\sim$2%. **The chlorine incorporation greatly enhances the diffusion coefficient of Li-ions through the material, which contributed to the improved performance. However, other effects, such as modifications to the electronic**

structure of TiO_{22} may influence the performance of TiO_2 coated LMO as well (e.g. through better band alignment between the active material and coating) can influence the performance (e.g. the effect on the Coulombic efficiency, activation behaviour,...).

A comparative peak analysis of CVs measured on TiO_2 and TiO_2Cl coated LMO, after galvanostatic charge-discharge indicates diffusion limited Li-ion insertion, wherein the diffusion limit is caused by the surface coating. The 3 V region was more severely affected by the addition of a surface coating than the 4 V region. Furthermore, TiO_2Cl coatings were shown to be less detrimental than TiO_2 for the entire thickness range from 1-5 nm. The disparate insertion kinetics between the 3 V and 4 V region could be attributed to the uniaxial lattice expansion in LMO due to a cubic to tetragonal phase transition. The addition of the coating can detrimentally affect the lattice straining through generation of contact stress. If the coating itself is not sufficiently malleable the lattice expansion of the electrode will be inhibited by the added contact stress at the interface between the active material and coating, which leads to a reduced capacity, and could be at the basis of the increased resistance.

Acknowledgement

The authors thank Praveen Dara and Johan Meersschaut for executing and analysing the ERD measurements, Johan Desmet and Johan Meersschaut for executing and analysing the RBS. Furthermore, the authors thank Kurt J. Lesker Company for supplying the Mini SPECTROS and Nano 36 glovebox cluster tool. L.D.T. gratefully acknowledges the support for the Ph.D. from the Research Foundation Flanders (FWO) scholarship (Grant No. 1S67818N).

References

(1) Gummow, R.; de Kock, A.; Thackeray, M. Improved capacity retention in rechargeable 4 V lithium/lithium-manganese oxide (spinel) cells. *Solid State Ionics* **1994**, *69*, 59 – 67.

(2) Abakumov, A. M.; Fedotov, S. S.; Antipov, E. V.; Tarascon, J.-M. Solid state chemistry for developing better metal-ion batteries. *Nature Communications* **2020**, *11*, 4976.

(3) Thackeray, M. M. Manganese oxides for lithium batteries. *Progress in Solid State Chemistry* **1997**, *25*, 1 – 71.

(4) Li, X.; Xu, Y.; Wang, C. Suppression of Jahn–Teller distortion of spinel LiMn2O4 cathode. *Journal of Alloys and Compounds* **2009**, *479*, 310 – 313.

(5) Yamada, A. Lattice Instability in Li(LixMn2-x)O4. *Journal of Solid State Chemistry* **1996**, *122*, 160 – 165.

(6) Bhandari, A.; Bhattacharya, J. Review—Manganese Dissolution from Spinel Cathode: Few Unanswered Questions. *Journal of The Electrochemical Society* **2016**, *164*, A106–A127.

(7) Kim, J.-H.; Pieczonka, N. P. W.; Yang, L. Challenges and Approaches for High-Voltage Spinel Lithium-Ion Batteries. *ChemPhysChem* **2014**, *15*, 1940–1954.

(8) Fu, L.; Liu, H.; Li, C.; Wu, Y.; Rahm, E.; Holze, R.; Wu, H. Surface modifications of electrode materials for lithium ion batteries. *Solid State Sciences* **2006**, *8*, 113 – 128.

(9) Jang, D. H.; Shin, Y. J.; Oh, S. M. Dissolution of Spinel Oxides and Capacity Losses in 4 V Li / Li x Mn2 O 4 Cells. *Journal of The Electrochemical Society* **1996**, *143*, 2204–2211.

(10) Amatucci, G.; Schmutz, C.; Blyr, A.; Sigala, C.; Gozdz, A.; Larcher, D.; Tarascon, J. Materials' effects on the elevated and room temperature performance of CLiMn2O4 Li-ion batteries. *Journal of Power Sources* **1997**, *69*, 11 – 25.

(11) Xiao, B.; Wang, P.-b.; He, Z.-j.; Yang, Z.; Tang, L.-b.; An, C.-s.; Zheng, J.-c. Effect of MgO and TiO2 Coating on the Electrochemical Performance of Li-Rich Cathode Materials for Lithium-Ion Batteries. *Energy Technology* **2019**, *7*, 1800829.

(12) Li, J.; Fan, M.; He, X.; Zhao, R.; Jiange, C.; Wan, C. TiO2 coating of LiNi1/3Co1/3Mn1/3O2 cathode materials for Li-ion batteries. *Ionics* **2006**, *12*, 215–218.

(13) Zhao, S.; Zhu, Y.; Qian, Y.; Wang, N.; Zhao, M.; Yao, J.; Xu, Y. Annealing effects of TiO2 coating on cycling performance of Ni-rich cathode material LiNi0.8Co0.1Mn0.1O2 for lithium-ion battery. *Materials Letters* **2020**, *265*, 127418.

(14) Kim, S.-J.; Kim, M.-C.; Kwak, D.-H.; Kim, D.-M.; Lee, G.-H.; Choe, H.-S.; Park, K.-W. Highly stable TiO2 coated Li2MnO3 cathode materials for lithium-ion batteries. *Journal of Power Sources* **2016**, *304*, 119–127.

(15) Jung, Y. S.; Cavanagh, A. S.; Riley, L. A.; Kang, S.-H.; Dillon, A. C.; Groner, M. D.; George, S. M.; Lee, S.-H. Ultrathin Direct Atomic Layer Deposition on Composite Electrodes for Highly Durable and Safe Li-Ion Batteries. *Advanced Materials* **2010**, *22*, 2172–2176.

(16) Mattelaer, F.; Vereecken, P. M.; Dendooven, J.; Detavernier, C. The Influence of Ultrathin Amorphous ALD Alumina and Titania on the Rate Capability of Anatase TiO2 and LiMn2O4 Lithium Ion Battery Electrodes. *Advanced Materials Interfaces* **2017**, *4*, 1601237.

(17) Yang, J.; Wang, Y.; Li, W.; Wang, L.; Fan, Y.; Jiang, W.; Luo, W.; Wang, Y.; Kong, B.; Selomulya, C.; Liu, H. K.; Dou, S. X.; Zhao, D. Amorphous TiO2 Shells: A Vital

Elastic Buffering Layer on Silicon Nanoparticles for High-Performance and Safe Lithium Storage. *Advanced Materials* **2017**, *29*, 1700523.

(18) Moitzheim, S.; De Gendt, S.; Vereecken, P. Investigation of the Li-Ion Insertion Mechanism for Amorphous and Anatase TiO2 Thin-Films. *Journal of The Electrochemical Society* **2019**, *166*, A1–A9.

(19) Chen, Z.; Qin, Y.; Amine, K.; Sun, Y.-K. Role of surface coating on cathode materials for lithium-ion batteries. *J. Mater. Chem.* **2010**, *20*, 7606–7612.

(20) Yu, F.; Du, L.; Zhang, G.; Su, F.; Wang, W.; Sun, S. Electrode Engineering by Atomic Layer Deposition for Sodium-Ion Batteries: From Traditional to Advanced Batteries. *Advanced Functional Materials* **2020**, *30*, 1906890.

(21) Chen, L.; Warburton, R.; Chen, K.-S.; Libera, J.; Johnson, C.; Yang, Z.; Hersam, M.; Greeley, J.; Elam, J. Mechanism for Al2O3 Atomic Layer Deposition on LiMn2O4 from In Situ Measurements and Ab Initio Calculations. *Chem* **2018**, *4*.

(22) Winter, M.; Brodd, R. J. What Are Batteries, Fuel Cells, and Supercapacitors? *Chemical Reviews* **2004**, *104*, 4245–4270, PMID: 15669155.

(23) Kim, J.-S.; Lee, D.-C.; Lee, J.-J.; Kim, C.-W. Optimization for maximum specific energy density of a lithium-ion battery using progressive quadratic response surface method and design of experiments. *Scientific Reports* **2020**, *10*, 15586.

(24) Put, B.; Vereecken, P. M.; Labyedh, N.; Sepulveda, A.; Huyghebaert, C.; Radu, I. P.; Stesmans, A. High Cycling Stability and Extreme Rate Performance in Nanoscaled LiMn2O4 Thin Films. *ACS Applied Materials & Interfaces* **2015**, *7*, 22413–22420, PMID: 26436688.

(25) Moitzheim, S.; Balder, J. E.; Poodt, P.; Unnikrishnan, S.; De Gendt, S.;

Vereecken, P. M. Chlorine Doping of Amorphous TiO2 for Increased Capacity and Faster Li+-Ion Storage. *Chemistry of Materials* **2017**, *29*, 10007–10018.

(26) De Taeye, L. L.; Mees, M. J.; Vereecken, P. M. Surpassing the 1 Li/Ti capacity limit in chlorine modified TiO2-yCl2y. *Energy Storage Materials* **2021**, *36*, 279 – 290.

(27) Yan, S.; Abhilash, K. P.; Tang, L.; Yang, M.; Ma, Y.; Xia, Q.; Guo, Q.; Xia, H. Research Advances of Amorphous Metal Oxides in Electrochemical Energy Storage and Conversion. *Small* **2019**, *15*, 1804371.

(28) Van der Ven, A.; Marianetti, C.; Morgan, D.; Ceder, G. Phase transformations and volume changes in spinel LixMn2O4. *Solid State Ionics* **2000**, *135*, 21 – 32, Proceedings of the 12th International Conference on Solid State.

(29) Sheth, J.; Karan, N. K.; Abraham, D. P.; Nguyen, C. C.; Lucht, B. L.; Sheldon, B. W.; Guduru, P. R. In Situ Stress Evolution in Li 1+x Mn 2 O 4 Thin Films during Electrochemical Cycling in Li-Ion Cells. *Journal of the Electrochemical Society* **2016**, *163*.

(30) Jeon, Y.; Noh, H. K.; Song, H.-K. A Lithium-ion Battery Using Partially Lithiated Graphite Anode and Amphi-redox LiMn2O4 Cathode. *Scientific Reports* **2017**, *7*, 14879.

(31) Oliver, W. C.; Pharr, G. M. An improved technique for determining hardness and elastic modulus using load and displacement sensing indentation experiments. *Journal of Materials Research* **1992**, *7*, 1564–1583.

(32) Rodríguez, M.; Molina-Aldareguía, J.; González, C.; LLorca, J. Determination of the mechanical properties of amorphous materials through instrumented nanoindentation. *Acta Materialia* **2012**, *60*, 3953–3964.

(33) Vaidyanathan, R.; Dao, M.; Ravichandran, G.; Suresh, S. Study of mechanical defor-

mation in bulk metallic glass through instrumented indentation. *Acta Materialia* **2001**, *49*, 3781–3789.

(34) Bishop, S.; Marrocchelli, D.; Chatzichristodoulou, C.; Perry, N.; Mogensen, M.; Tuller, H.; Wachsman, E. Chemical Expansion: Implications for Electrochemical Energy Storage and Conversion Devices. *Annual Review of Materials Research* **2014**, *44*, 205–239.

(35) Koyama, Y.; Chin, T.; Rhyner, U.; Holman, R.; Hall, S.; Chiang, Y.-M. Harnessing the Actuation Potential of Solid-State Intercalation Compounds. *Advanced Functional Materials* **2006**, *16*, 492–498.

Supporting information

XRD measurements were conducted on 40 nm TiO_2 samples deposited at different temperatures. Herein, we saw no additional diffraction peaks in samples deposited at higher chamber temperatures.

Crystallization to anatase and rutile phase are not expected at temperatures below 300^{o}C and 900^{o}C, respectively. As such we expect the amorphous phase to be preserved in both these films.

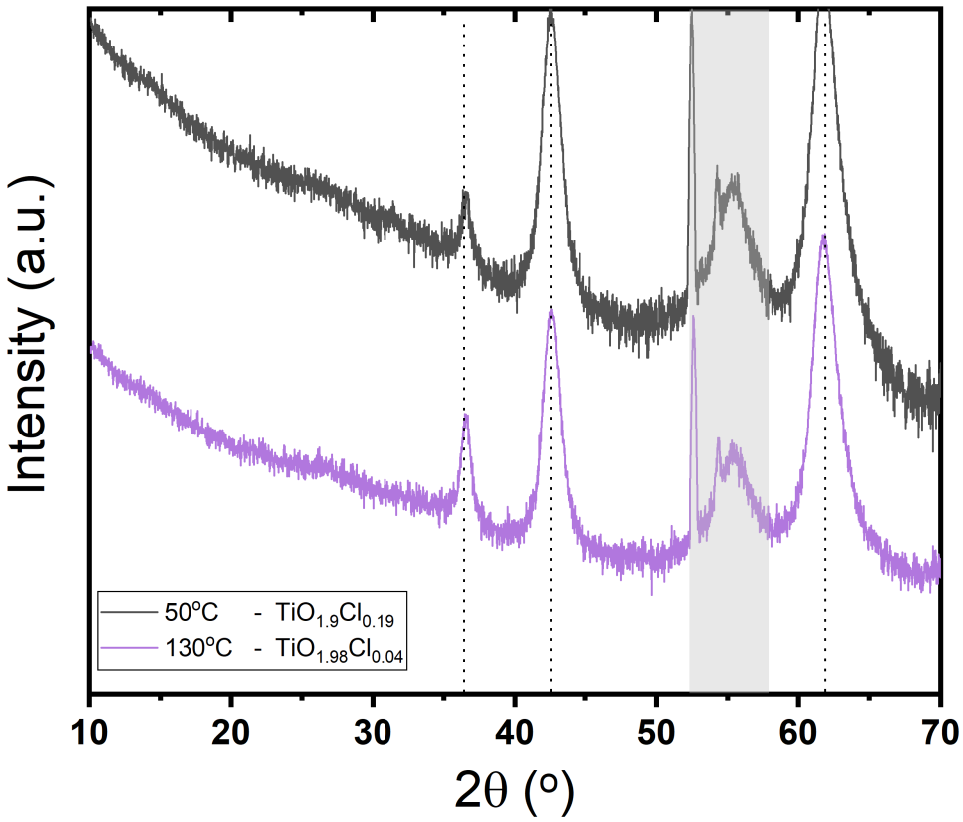

Figure 8: XRD diffraction patterns of 40 nm highly and lowly chlorine modified TiO_2 films deposited at 50^{o}C and 130^o C, respectively.

Figure 9 shows the Coulombic efficiency of all charge-discharge cycles shown in figure 4. The grey boxes indicate the cycles after a change in the charging rate. This value

does not reflect the actual charging efficiency, as it is influenced by the change in charging rate. A trend towards increasing efficiency is primarily observed in the initial cycles of the reference measurement and the sample with a 1 nm coating. The TiO_2Cl samples show constant stability throughout the procedure. For the 3 nm TiO_2 coating, a strong variance is observed during the initial cycles, which is linked with the activation behaviour shown in figure 4c. Only after reaching a stable charge-discharge plateau, does the efficiency stabilize. The trend observed in the final four cycles, namely where LMO with thicker coatings is more efficient, is observed throughout the whole procedure. Further, we see that at higher C-rates the charging efficiency is higher. This is the consequence of the reduced duration of the charge-discharge cycles. At elevated potentials, a parasitic oxidation current will flow. This current leads to an excess charge during the charging step and a charge loss during the discharging step. The total excess or loss scales with the duration of the (dis)charge step.

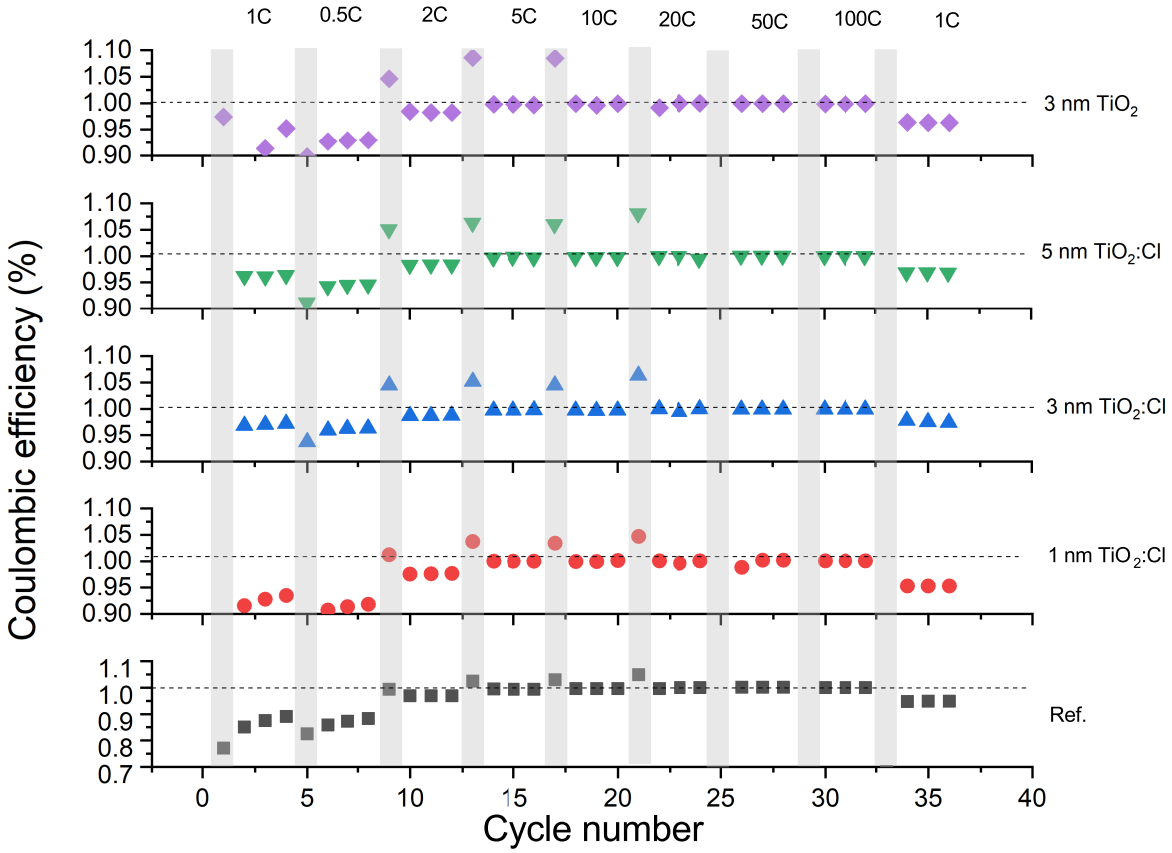

Figure 9: Coulombic efficiencies of all cycles measured in the charge-discharge procedure (Fig. 4).